Volume 1 | Number 1 | Jan 2013 | Pages 1–100

Soft Matter

www.rsc.org/softmatter

ROYAL SOCIETY OF CHEMISTRY

This is an *Accepted Manuscript*, which has been through the Royal Society of Chemistry peer review process and has been accepted for publication.

Accepted Manuscripts are published online shortly after acceptance, before technical editing, formatting and proof reading. Using this free service, authors can make their results available to the community, in citable form, before we publish the edited article. We will replace this *Accepted Manuscript* with the edited and formatted *Advance Article* as soon as it is available.

You can find more information about *Accepted Manuscripts* in the **Information for Authors**.

Please note that technical editing may introduce minor changes to the text and/or graphics, which may alter content. The journal's standard **Terms & Conditions** and the **Ethical guidelines** still apply. In no event shall the Royal Society of Chemistry be held responsible for any errors or omissions in this *Accepted Manuscript* or any consequences arising from the use of any information it contains.

ENTROPIC SELF-ASSEMBLY OF FREELY ROTATING POLYHEDRAL PARTICLES CONFINED TO A FLAT INTERFACE

V. Thapar, T. Hanrath, and F. A. Escobedo*
School of Chemical and Biomolecular Engineering, Cornell University
Ithaca New York 14853

AUTHOR EMAIL ADDRESS (*fe13@cornell.edu)

Abstract

The self-assembly of hard polyhedral particles confined to a flat interface is studied using Monte Carlo simulations. The particles are pinned to the interface by restricting their movement in the direction perpendicular to it while allowing their free rotations. The six different polyhedral shapes studied in this work are selected from a family of truncated cubes defined by a truncation parameter, s, which varies from cubes ($s = 0$) via cuboctahedra ($s = 0.5$) to octahedra ($s = 1$). Our results suggest that shapes with small values of s show square-like behavior whereas shapes with large values of s tend to show more disc-like behavior. At an intermediate value of $s = 0.4$, the phase behavior of the system shows both square-like and disc-like features. The results are also compared with the phase behavior of 3D bulk polyhedra and of 2D rounded hard squares. Both comparisons reveal key similarities in the number and sequence of mesophases and solid phases observed. These insights on 2D entropic self-assembly of polyhedral particles is a first step toward understanding the self-assembly of particles at fluid-fluid interfaces, which is driven by a complex interplay of entropic and enthalpic forces. A first-order analysis of the particle-surface energies associated with a fluid-fluid interface indicate that such enthalpic interactions will be particularly important in determining particle orientation behavior at low to intermediate concentrations.

1. Introduction

At present, a major focus in material science is the use of polyhedral colloidal nanoparticles as versatile building blocks to design and fabricate novel materials with targeted emergent properties. Remarkable strides have been made in experimental techniques[1-6] to synthesize these building blocks with different sizes, shapes, compositions and patterns. Understanding the relationship between particle shape and structural order is crucial for materials design because of the dependence of physical properties on the structure. This has fueled many theoretical[7,8] and simulation studies[9-21] of polyhedral particles to map out their phase behavior. These systems often undergo order-disorder phase transitions involving changes in both translational and orientational degrees of freedom and can lead to novel mesophases. A mesophase is a partially ordered phase whose properties are intermediate between those of disordered liquids and ordered crystals, such as liquid crystals, rotator plastic crystals, and quasicrystals.

Some of the techniques to assemble polyhedral nanoparticles involve the use of fluid interfaces as templates. The idea of using fluid interfaces was first explored for micron-sized particles by Pickering[22] and Ramsden[23] when they investigate paraffin water emulsions with solid particles of various oxides, salts, and clays. They found that these colloids generate a resistant film at the paraffin-water interface inhibiting the coalescence of the emulsion drops. These so-called Pickering emulsions are formed by the self-assembly of colloidal particles at fluid-fluid interfaces[24]. During these past years, several studies[25-37] have focused on using this directed self-assembly technique to synthesize

two-dimensional (2D) superstructures of anisotropic particles. These quasi-2D superstructures provide a valuable experimental testbed to study extended electronic properties and have broad technological potential in applications involving thin-film optical and electronic devices[29,30,38,39].

To establish a robust framework to control the self-assembly of nanoparticles at fluid interfaces, a fundamental understanding of the interplay between entropic and enthalpic driving forces is critical. For this purpose, it is instructive to split the study into various complementary steps. The first step would involve simulating a model that isolates entropic effects only. A subsequent step would involve studying a model that also incorporates enthalpic effects like interfacial particle-fluid interactions to assess whether or how specific interactions reinforce or oppose entropic trends. In this work, we focus on the first-step entropic model where nanoparticles are described as perfect, monodisperse, hard polyhedral shapes so that their preferential packing is only dictated by excluded volume interactions. In our model, the particles' centers of mass are pinned to a flat interface such that they cannot translate in a direction perpendicular to that interface, but they are allowed to translate on the surface and rotate freely. The lack of translational freedom in one direction restricts the system of 3D particles to pack in a quasi-2D space and hence we refer to this assembly as 2D confined self-assembly. We use this model to simulate the phase behavior of several shapes belonging to a family of truncated cubes as characterized in ref. 17. Specifically, the shapes studied are cubes, truncated cubes (TCs), truncated cubes with truncation parameter s=0.4 (TC4s), cuboctahedrons (COs), truncated octahedrons (TOs) and octahedrons (Octs). These choices are motivated by both their relevance to experimental studies[2,3,29,30] and the availability of reference simulation results for the 3D entropic self-assembly[17]. Our work is also related to previous simulation studies on the phase behavior of true 2D systems, in particular, of rounded hard squares [40], where particular cases bear some shape-similarity with our shapes when projected in 2D. The key difference between this work and that of ref. 40 is that the shapes studied here are fully three-dimensional (e.g., cubes rather than squares).

By way of background, in Section 2 we explain the methodology used to outline the phase behavior of each polyhedron, along with the relevant order parameters used to distinguish different phases. In Section 3, we report the results for the different shapes studied in this work along with the comparisons with the 3D bulk phase behavior and the 2D phase behavior of rounded hard squares[40]. Finally, in Section 4 we provide some concluding remarks.

2. Methodology

To confine the self-assembly of the particles in 2D, we fix the z-coordinate of the center of mass of each particle and only allow translations in the x and y direction. We perform extensive expansion and compression Monte Carlo (MC) runs in the isothermal-isobaric NPT ensemble (N is number of particles) with standard periodic boundary conditions to map out the equation of state (EoS) for each shape. In our simulations, we assume the particles interact via hard core potential, which forbids particles from overlapping. Each pressure step of expansion/compression involved a run of 3×10^6 MC cycles in total, with the first 2×10^6 MC cycles used for equilibration and the latter 10^6 MC cycles used for production. Each MC cycle consists of an average of N translational, N rotational, N/10 flip and 1 area change move attempts. Flip moves attempt to rotate a chosen particle to a random orientation in the plane perpendicular to its present orientation. As indicated before, translational moves are only allowed in x and y direction. At high densities, area moves are allowed to also change the angle between the box axes to relieve internal stresses and avoid the formation of artificial phases due to a fixed square box symmetry. All trial moves are accepted according to the Metropolis criterion[41], which requires ruling out overlaps between any two particles (via the separating axes theorem[42]). The size of

the move perturbations is adjusted so as to get acceptance probability values of 0.4, 0.4 and 0.2 for the translation, rotation and volume moves, respectively.

The formation of ordered phases is detected using several global order parameters. The bond order parameters ψ_4 and ψ_6 are used to detect four-fold and six-fold angular order, respectively. For each particle, identified by j, we define a complex number, the local n-fold bond orientational order $\varphi_n(\mathbf{r_j})$:

$$\varphi_n(\mathbf{r_j}) = \frac{1}{n_j}\sum_{k=1}^{n_j}\exp(in\theta_{jk}) \qquad (1)$$

for $n = 4$ and 6. In the above equation, θ_{jk} is the angle made by bond between particle j and its nearest neighbor k with respect to an arbitrary axis, and n_j is the number of nearest neighbors of particle j. For $\varphi_6(\mathbf{r_j})$, n_j is calculated using Voronoi tessellation, while for $\varphi_4(\mathbf{r_j})$ the four closest neighbors of each particle are used. The magnitude of $\varphi_n(\mathbf{r_j})$, estimates the value of local n-fold bond orientational order, φ_n^j for particle j. The global bond orientational order, ψ_n for N particles is the magnitude of the average of $\varphi_n(\mathbf{r_j})$ as defined below

$$\psi_n = \left|\frac{1}{N}\sum_{j=1}^{N}\varphi_n(\mathbf{r_j})\right| \qquad (2)$$

The global particle orientational order in the system is determined via the P_4 cubic order parameter defined as[43]

$$P_4 = \max_{n}\frac{1}{N}\sum_{i}P_4(\mathbf{u_i}\cdot\mathbf{n})$$
$$= \max_{n}\frac{1}{8N}\sum_{i}(35\cos^4\tau_i(\mathbf{n}) - 30\cos^2\tau_i(\mathbf{n}) + 3) \qquad (3)$$

where, $\mathbf{u_i}$ is the unit vector along a relevant particle axis and $\mathbf{n}$ is a director unit vector which maximizes P_4 (see details in ref. 9). The spatial range of orientational order is quantified using the orientational distribution function $I_4(r)$[12], defined as

$$I_4(r) = \frac{1}{8N}\left\langle 35[\mathbf{u_{ai}}(0)\cdot\mathbf{u_{bi}}(\mathbf{r})]^4 - 30[\mathbf{u_{ai}}(0)\cdot\mathbf{u_{bi}}(\mathbf{r})]^2 + 3\right\rangle \qquad (4)$$

where the average is over all particle pairs and all nine combinations of the axes. Translational order is detected by analyzing the behavior of the radial distribution function $g(r)$, the structure factor, $S(\mathbf{k})$, defined as

$$S(\mathbf{k}) = \frac{1}{N}\left\langle\left[\sum_{i=1}^{N}\cos(\mathbf{k}\cdot\mathbf{r}_i)\right]^2 + \left[\sum_{i=1}^{N}\sin(\mathbf{k}\cdot\mathbf{r}_i)\right]^2\right\rangle, \qquad (5)$$

and the bond orientational correlation function given by

$$g_k(\mathbf{r}) = <\varphi_k(0)\varphi_k(\mathbf{r})> \qquad (6)$$

where $\varphi_k(\mathbf{r})$ is the k-fold local bond orientational order at position $\mathbf{r}$.

The regions of phase stability for a given system are outlined by mapping out the EoS via compression and expansion runs. The compression runs were started using a low density isotropic state with negligible translational and orientational order, and continued until attaining the high-density crystalline phase. As discussed in ref. 44, the crystal phase for 2D systems lacks true long-range translational order (unlike 3D systems), which means that the translational correlations of the crystal phase decay algebraically to zero. However, the system sizes studied here are not large enough to observe this decaying behavior. The resulting phase is then used as a starting point for expansion runs.

To detect the points where phase transitions occur, we looked for not only breaks and inflections points in the EoS curves, but also for spots where fluctuations of bond order parameters, defined as

$$\chi_n = N\left(\left\langle \psi_n^2 \right\rangle - \left\langle \psi_n \right\rangle^2\right) \tag{7}$$

diverge or have larger peaks[45]. The latter has been found to be less sensitive to finite size effects than the former[40,46]. Since the EoS and transition points found by compression and expansion runs exhibited little hysteresis and we are only interested in outlining approximate boundaries, we did not perform complementary (and costly) free energy calculations.

We use conventional reduced units to report our results for the phase behavior of different shapes. The truncation parameter,[17] s for cubes, TCs, TC4s, COs, TOs, and Octs is 0, $(2-\sqrt{2})/2$, 0.4, 1/2, 2/3 and 1 respectively. The reduced pressure, P^* is defined as $P^* = Pa^2/(k_BT)$ where $2a$ is the diagonal of the (imaginary) cube from which the given shape is cut. k_B is Boltzmann constant and T is absolute temperature. The reduced number density is defined as $\eta = Na^2/A$, where A is the total area of the system. We report our results in normalized reduced number density, $\eta^* = \eta/\eta^{crys}$ where η^{crys} is the reduced number density of a crystal phase for $N = 1600$ particles at a very high pressure, namely, $P^* = 500$ (η^{crys} essentially correspond to the densest packing state).

3. Results

3.1 Cubes ($s = 0$) and TCs ($s = 0.293$)

For cubes, most simulations entailed a system size of $N = 1600$ particles. The EoS results are shown in Fig.1 including data for a smaller $N = 400$ particle system for comparison. The EoS for the small and large systems from expansion runs matches well for the entire range of densities. We also observed a similar trend for the compression runs of the same system (not shown). At low concentrations, all the order parameters have values close to zero, which is characteristic of the isotropic phase. Around $\eta^* \approx 0.55$, the values of ψ_4 and P_4 start increasing with pressure while the value of ψ_6 stays close to zero. At $\eta^* \approx 0.9$, ψ_4 and P_4 reach their maximum values, which are consistent with a crystal with square order. A similar isotropic to square phase transition is also observed for a larger system size with $N = 3600$ and has also been observed before in hard squares[47] and rounded hard squares with small corner to length rounding ratios[40]. In the phase behavior of hard squares, ref. 47 shows that the system goes from isotropic to square phase via an intermediate phase referred to as tetratic phase. As described in ref. 40 and ref. 47, the tetratic phase has significant particle orientational and four-fold bond orientational order, but $g(r)$ shows short-range positional ordering (no peaks at large distances) and the structure factor $S(\mathbf{k})$ exhibits diffusive peaks with four-fold symmetry. These tetratic-like properties are observed in our case for a region intermediate between the isotropic and square phases. As shown in Fig. 1. for $0.6 < \eta^* < 0.7$, one observes that $0.4 < \psi_4 < 0.8$, and $0.4 < P_4 < 0.45$ whiled the coupling between particle orientations and (nearest neighbor) bond orientations also increases rapidly as detected by the cross parameter ψ_4P_4. As shown in Fig. 2, at these conditions $S(\mathbf{k})$ exhibits diffuse peaks with four fold symmetry and $g(r)$ shows short-range ordering consistent with tetratic-like behavior. For comparison, we also show in Fig. 2 plots of the structure factor plot and $g(r)$ for the square phase. The lack of any translational degrees of freedom in z-direction in our model renders the behavior of hard cubes similar to that of hard squares. We also compare this self-assembly of cubes confined in 2D to the self-assembly of cubes in the bulk in 3D[12,17]. Besides the expected differences in the symmetry of the densest packings (square in 2D and cubic in 3D), we also find that at least for the system sizes studied here cubes undergo a continuous phase transition from isotropic to square phase which differs from the first order phase transition from isotropic to simple cubic phase observed in

bulk 3D self-assembly. The pseudo 2D phase behavior of TCs is very similar to that of cubes and is described in the supplementary material[48].

3.2 TC4s ($s = 0.4$)

As shown in Fig. 3, a system of $N = 1600$ T4Cs transitions from isotropic to square phase via two intermediate mesophases. Firstly, the system undergoes a transition from isotropic to a phase with partial six fold bond orientational order and no particle orientational order, which, on further increasing the pressure, loses its six fold symmetry and gains both four fold bond orientational order and particle orientational order. Further compression of the system results in a crystalline square phase. We observe a similar phase behavior for a larger system sizes with $N = 3600$ (results not shown). To better understand the two intermediate phases, we first look at the phase with $\psi_6 \approx 0.45$ observed for $0.65 < \eta^* < 0.69$ and find that its $S(\mathbf{k})$ shows diffuse peaks with six-fold symmetry (see Fig. 4b). The corresponding correlation function $g_6(r)$ (Fig. 5) shows long-range partial hexatic order whereas $g(r)$ shows a quick decay of the peak amplitudes with distance, indicative of short-range translational order. These properties are consistent with those of the hexatic phase observed in the case of hard discs. We note, however, that hexatic character could only be unambiguously determined with a scaling analysis involving much larger system sizes than those used here, a task that lies beyond the scope of this work. For the other intermediate phase observed in $0.71 < \eta^* < 0.76$, $S(\mathbf{k})$ exhibits diffuse four-fold peaks, $g_6(r)$ and $I_4(r)$ reveal long-range partial tetratic bond orientational and particle orientational order, and $g(r)$ indicates a short-range translational order (see Figs. 4 and 5). This intermediate phase has similar properties to those of the transitional phase observed before in cubes and TCs when the system transitions from isotropic to square phase. The absence of breaks in order parameters and η^* vs. pressure as the system transitions between phases suggests that the transitions are continuous. Interestingly, similar to the phases observed here for TC4s confined in 2D, the bulk self-assembly of TC4s in 3D also exhibits an intermediate mesophase with six-fold symmetry and a densest packing phase with a different symmetry.[17]

3.3   COs ($s = 0.5$)

The EoS for $N = 1600$ COs is shown in Fig. 6. The system undergoes a phase transition from isotropic to a hexagonal rotator phase characterized by high six-fold bond orientational order and negligible particle orientational order. This transition is accompanied by discontinuities in the values of η^* and ψ_6, suggesting that the transition would be first order. The hexagonal rotator phase in the range of $0.67 < \eta^* < 0.77$ shows sharp $S(\mathbf{k})$ peaks of hexagonal symmetry which is in line with the solid-like positional ordering (peaks persisting to large distances) behavior detected in $g(r)$ (see Fig. 7). By further increasing the density, the system transitions from a hexagonal rotator phase to a crystal phase having high particle orientational order and a distorted translational symmetry. The $g(r)$ of the crystal phase has a solid like behavior as shown in Fig. 7 but the $S(\mathbf{k})$ plot shows that system has neither fully six-fold nor four-fold symmetry. To better understand this crystal phase, we calculate φ_4^j and φ_6^j for each particle and show in Fig. 10 a snapshot of the system at $P^*=59.4$ by coloring the particles based on their (local) values of φ_4^j and φ_6^j [as per Eq. (1)]. The system has mainly hexagonal-like character which is consistent with a high global $\psi_6 \sim 0.85$, but also has layers of four-fold symmetry, indicating some localized interlocking between phases with six fold and four fold symmetry. A similar interlocking between phases has also been observed in the simulated crystal phase of COs assembling in 3D[17]. Also, COs in 3D exhibit isotropic, hexagonal rotator phase and a crystal phase with a distorted lattice upon compression, a sequence of phases that is loosely "equivalent" to that we observed in 2D.

3.4 TOs (*s* = 2/3)

The phase behavior of TOs for a system of $N = 1600$ particles is shown in Fig. 9. As can be observed, the EoS for $N=400$ and $N=1600$ agree very well and reveal two phase transitions. The first one, observed at $\eta^* \approx 0.6$, is the transformation from an isotropic phase to hexagonal rotator phase characterized by a large increase in ψ_6. The second transition observed at $\eta^* \approx 0.83$ is the transformation from hexagonal rotator phase to rhombic phase, that latter characterized by large values of ψ_4, ψ_6 and P_4. Figure 10 shows representative snapshots of both hexagonal rotator phase and rhombic phase including the corresponding structure factors. The difference in hexagonal rotator phase and rhombic phase can also be observed by plotting the distributions of angles, α, made by the vector joining an ith particle and its closest neighbor with the vector joining an ith particle and its next five closest neighbors (where neighbors are identified via Voronoi tessellation). As expected, for the hexagonal rotator phase this angular distribution peaks at 60, 120 and 180 degrees. In contrast, for the rhombic phase we see 5 peaks at around 55, 70, 110, 125 and 180 degrees. The discontinuities in order parameters and η^* for the two phase transitions suggest that they are both first order.

The phases observed for this case are similar to the 2D phases observed for rounded hard squares with high corner to length rounding ratios[40]. Similar to the confined case studied here, a transition akin to isotropic-to-rotator phase is also observed in the self-assembly of TOs in 3D[12,17], but unlike our observation of particles abruptly aligning to transform from rotator phase to rhombic phase, a continuous transition from orientationally disordered rotator phase to bcc phase is observed in 3D.

3.5 Octs (*s* = 1)

The phase behavior of Octs for $N =1600$ particles is shown in Fig. 11. The discontinuity in the order parameter values of ψ_4, ψ_6 and P_4 and η^* around $\eta^* \approx 0.67$ suggests that the system transforms into a hexagonal crystal phase via a first-order transition. A representative snapshot of the hexagonal crystal phase along with its corresponding structure factor and radial distribution function are shown in Fig. 12. We observe sharp $S(\mathbf{k})$ peaks with six-fold symmetry for the hexagonal crystal phase, consistent with the solid-like behavior detected in $g(r)$. Over a short density range before $\eta^* \approx 0.67$ the system has no particle orientational order (low P_4 values) but has non negligible values of ψ_4 and ψ_6, which we associate with a novel mesophase that we'll denote as a "dimorphic" rotator. The same phase is observed in expansion and compression runs for $N = 3600$ particles. As shown in Fig.12 for $N = 3600$ particles, the structure factor plot of this mesophase reveals diffuse peaks with no clear symmetry while $g(r)$ shows small but persistent peak at long distances. To try to further characterize the structure of this phase, we visually analyzed sample configurations by coloring the particles based on their individual values of φ_4^j and φ_6^j [see Eq. (1)]. As Figure 13 shows, this mesophase has a grainy character where two kinds of "grains" intermingle (hence the name dimorphic): some are patches of particles having high six-fold symmetry and low four-fold symmetry, while others are patches of particles having high four-fold and low six-fold symmetry. While this dimorphic phase bears some similarity to the so-called polycrystalline phase detected for a small range of concentrations and roundedness parameter in rounded squares[40], it seems to have less translational order.

3.6 General trends of behavior

Figure 14 summarizes the phase behavior for all the shapes studied here. As the value of *s* is increased, the range of densities at which a phase with six-fold symmetry is stable increases and the reverse trend

ensues for a phase with four-fold symmetry. Based on this approximate trend, one would expect that the two-body potential of mean force (*PMF*) of the different shapes may reveal some signs for a stronger disc-like behavior with increasing *s*. Hence, we estimate one-dimensional and two-dimensional *PMFs* at different values of *s* using the procedure mentioned in ref. 48. As expected, the one-dimensional *PMF(r)* shape (Fig. S3 in the supplementary material[48]) has a more compact repulsive tail and shorter range (i.e., more disc-like character) for shapes with larger *s,* although this trend is somewhat reversed between COs and Octs. The *PMF(r)* shape of Octs for larger values of *r* (>1.15) is intermediate between those for COs and TCs, which would be consistent with an intermediate proclivity toward disk-like and square-like behavior as embodied by the novel dimorphic phase formed by Octs. The two-dimensional *PMF(x,y)* (Fig. S4 in the supplementary material[48]) allows visualization of the asymmetry in the effective two-particle interactions along their relative (in-plane) orientations. For any such orientation, the value of *βPMF(x,y)* decays faster over distance from large repulsion (*βPMF(x,y)* ≥ 5) to no repulsion for shapes with larger *s*, which is consistent with the trends seen in *PMF(r)*. Also, the TOs' *PMF(x,y)* has a marked circular-like symmetry which is consistent with the hexagonal rotator phase that was detected for a wide range of densities.

Besides summarizing the wide variety of phases we observe for different values of *s*, Figure 14 also gives a sense for how such phases are related across shapes and provides some clues as to how different phase types could be interpolated (for shapes whose *s* we did not simulate). We observe that for each phase observed in our quasi 2D systems, a counter part is almost always identifiable in the 3D bulk phase behavior from ref. 17, in particular, the number and sequence of mesophases and solid phases match well for the systems simulated. Of course that lattice symmetries in the mesophases and crystal phases are necessarily different between the 3D and quasi-2D systems; further, the character of the phase transitions (first-order or continuous) either did not always corresponds or could not be unambiguously determined in our systems. Table 1 shows the approximate phase correspondences (ignoring the isotropic phase). The only mesophase that appears to have no counterpart in the 3D case is the dimorphic mesophase we found in Octs.

The phase behavior of our systems also has some similarities with that of rounded squares. Arguably, the degree of truncation embodied by each shape could potentially be mapped to an effective degree of square roundedness, corresponding perhaps to the average projection of the shape onto the 2D pinning plane or to some key similarity in their *PMF*s. However, such a mapping would be flawed, since such a roundedness parameter would depend on concentration (unless a fixed particle orientation with respect to the interface could be assumed) for a given particle shape. Nonetheless we observe some correlation between the corner-rounding-to-length ratio, ζ (a parameter used to characterize the roundness of particles in ref. 40) and a parameter, λ_{shape} for our 3D shapes, defined as

$$\lambda_{shape} = \frac{a_{cube} - a_{shape}}{a_{cube} - a_{sphere}} \qquad (8)$$

where a_{shape}, a_{cube} and a_{sphere} is the asphericity of a given shape, cube and sphere respectively, which is defined as the ratio of circumdiameter σ_{out} to indiameter σ_{in}.[11] (for TC4 σ_{out} is the largest circumscribing diameter). The asphericity values for all the shapes are the same as the 'range' of the *PMF* (i.e., the smallest reduced distance r/σ_{in} for which *PMF(r)* = 0, see Fig. S3 of supplementary material[48]). To compare our results with those for rounded hard squares, the parameter λ_{shape} is a better metric than the truncation parameter *s*, as the degree of roundness increases with λ_{shape}. Table 1 also shows a comparison of phase behavior for some comparable values of λ_{shape} and ζ. At larger values of λ_{shape} and ζ, both types of systems show more disc-like behavior whereas at smaller values of λ_{shape} and ζ, the systems exhibit square-like phase behavior. However, this trend does not hold true for Octs,

which have the same λ_{shape} as cubes, but their phase behaviors are entirely different. This could be explained by the fact that although $PMF(r)$ of Octs and cubes decay to zero at the same value of r, their shapes are significantly different. We also observe a marked similarity in the phase behavior for some values of λ_{shape}, like for the $\lambda_{shape} = 0$ and $\zeta = 0$ cases, where both systems go from isotropic to a tetratic phase and then to a square phase. Also, when both λ_{shape} and ζ have a value close to 0.6, the systems undergo a transition from isotropic to hexagonal rotator phase followed by a transition to a rhombic phase.

3.7 Exploring the Contributions of Interfacial Energy

In our simulations, particles were restricted to translation over a 2D interface while allowing free rotations. However, surface forces strong enough to pin the z-coordinate of the center of mass of a particle may also bias the system toward some preferential orientations. For particles at the interface between fluids 1 and 2, the interfacial energy originating from the interactions between particle and fluid 1, particle and fluid 2, and between the two fluids will have an important effect on particle rotational behavior. To estimate such effects, we apply a continuum model used in refs. 30 and 31 to obtain the interfacial energy of a single particle at fluid 1/fluid 2 interface based on the properties of two fluids and a particle. For a given experimentally measured contact angle, θ_i corresponding to the three-phase contact between facet of type i ($i = 1,2$ for {100} and {111} facets respectively), fluid 1 and fluid 2, the model obtains the interfacial energy landscape based on the different polar angles (δ), azimuthal angles (ω), and immersion depths (z), of a particle relative to the fluid-fluid interface. The details for the estimation of interfacial energy F are provided in supplementary material[48].

For concreteness, we apply first the above model to a cubic particle with $\sigma_{out} \approx 3$ nm on a toluene air interface (which is commonly used for interface-mediated particle self-assembly.[31,49,50]). The effect of particle size on interfacial interactions is discussed later. Figure S5 in the supplementary material[48] shows the variation of interfacial energy, $F_{min}(z)$, minimized with respect to polar and azimuthal angles, as a function of immersion depth for different contact angles. The minimum in $F_{min}(z)$ occurs at $z = z_{opt}$. The interfacial energy barriers required to allow "vertical" translations (along the z-axis) are the highest for $\cos(\theta_1) = 0$, with z_{opt} corresponding to the particle center of mass being coplanar with the toluene-air interface; energy barriers for motion are moderate (with a value of $\sim 30k_BT$ relative to the fully immersed state but less than 5 k_BT for fluctuation of $\pm10\%$ the circumradius around z_{opt}) indicating that pinning at z_{opt} would be a reasonable approximation. On increasing $\cos(\theta_1)$, there is a decrease in the interfacial energy required for z-direction translations. A similar behavior is seen for other shapes, indicating that the assumption of fixed center-of-mass immersion length is most justified for values of $\cos(\theta_i)$ close to 0. For the choice of $\cos(\theta_1) = \cos(\theta_2) = 0$, we further obtain a metric denoted by ΔF_{orient}, intended to quantify how easily the particles can explore their orientational space. ΔF_{orient} is the difference between the interfacial energy of a configuration at a given polar and azimuthal angles and that of the minimum energy configuration, having all the same z_{opt} found before. Figure S6 in the supplementary material[48] shows ΔF_{orient} as a function of polar and azimuthal angles for different shapes with sizes chosen to have the same surface area of 18 nm^2 as the 3nm cube. Therefrom, we obtain the scalar metric, P_{orient}, defined as the percentage of angular phase space with $\Delta F_{orient} <= 5k_BT$. [48] The values of P_{orient} are 46, 64, 53, 15, 73 and 13% for cube, TC, TC4, CO, TO and Oct, respectively, showing that the extent of orientational bias towards the most stable (minimum-F_{min}) configuration is higher for shapes like Oct and CO and milder for TO and TC4. Also importantly, because of the particle rotational symmetry (number of rotations reproducing the same orientation), the most favorable orientation is always degenerate, indicating that particles could also dynamically rotate to access those states. We also observe that the most stable orientations (marked by

white portions in Fig. S6) strongly depend on particle shape. For a cube, the normal of one of the {110} facets parallel to the *z*-axis is the preferred orientation. Going from cubes to COs, the preferred orientation shifts to one where the normal of a {111} facet is parallel to the interface normal. On further increasing the truncation parameter, the preferred orientation for TO and Oct corresponds to that in which the normal of a {100} facet is parallel to the interface normal. Although both TO and Oct have the same most stable orientation, TO can explore orientations more freely than octahedra as observed in Fig. S6. This could be explained by the fact that TO (with a_{shape} = 1.291) has smaller asphericity than Oct (a_{shape} = 1.732).

The above analysis depends on the size/surface area of the particle since both ΔF_{min} and ΔF_{orient} are $\sim\sigma_{in}^{2}$. An *n*-fold increase in particle surface area would increase by a factor of *n* the interfacial energy required for both rotations and vertical translations. For these sizes, the interplay between orientational biasing fluid particle forces and entropic forces will depend on the concentration of the particles. To gain some insights into this interplay, we revisit the purely entropic case to see how concentration affects the extent of particle alignment with respect to the interface by measuring the order parameter P_{surf} defined as

$$P_{surf} = \frac{1}{8N}\sum_{i}(35\cos^{4}\Omega_{i} - 30\cos^{2}\Omega_{i} + 3) \qquad (9)$$

where, Ω_{i} is the angle between interfacial normal and one of the three {100} particle axes whose dot product with the interfacial normal is maximum. P_{surf} ranges from -0.42 to 1.0 and is $\sim$ 0 for random orientations and unity for parallel alignment with the interface. Figure 15 shows P_{surf} as a function of $\eta*$ for different shapes. At low $\eta*$, P_{surf} ~0 regardless of shape, indicating random alignment of particles relative to the interface. Small values of P_{surf} also correlate with the smaller values of $PMF(r)$ for large inter-particle distances (associated with small $\eta*$), which signal negligible inter-particle entropic forces. At these conditions the addition of enthalpic interfacial energy will strongly bias the orientations towards those of minimum interfacial energy. But at high $\eta*$ near the densest packing phase, the absolute value of P_{surf} is large signifying that the particles adopt particular orientations relative to the interface that maximize packing entropy. The strength of these entropic forces is also evident from the shape of PMF where for small interparticle distances r, $PMF(r)$ becomes very large. Since $(r/\sigma_{in})^{2} \approx \eta^{crys}/\eta = 1/\eta^{*}$, we can estimate from Fig. S3 that to have $PMF>5k_{B}T$ one would need $r/\sigma_{in} < 1.1$ and thus for $\eta*>0.8$ entropic forces should override any energetic orientational bias, so that the "entropic" solid phases we found would also correspond to the equilibrium states. Experimentally, reported instances refer to near closed-packed structures ($\eta*>0.8$) whose symmetries are consistent with those found in our model, e.g., for the PbSe nanocubes of ref. 30, square symmetry is observed at high concentrations, consistent with Fig. 1. Finally, Fig. 15 (right panel) also indicates that the single-particle lowest surface-energy orientation need not agree with that of particles in the densest packed solid, indicating that assuming a fixed particle orientation (relative to the interface) for all $\eta*$ would not generally be a suitable approximation.

In sum, while contact angles and particle sizes can be selected to approach the 2D freely rotating scenario simulated in this paper, interfacial energies will generally introduce non-trivial biases which may lead to different phase behaviors, particularly at low to intermediate densities. It is important to note that this analysis is based on a simple model that ignores the effects of interface deformations, line tension, fluid-facet-specific interactions, and interparticle enthalpic interactions (which may facilitate or restrict particle rotations and translations).

9

4. Conclusions and Discussion

In this work, we have simulated the confined 2D phase behavior of 6 different shapes, from cubes to octahedra, which belong to a family of truncated cubes often encountered in nanoparticle synthesis. The phase behavior of different shapes shows diversity in the type of mesophases and crystalline phases that form as concentration increases. Shapes with small values of s (cubes and TCs) shows a square-like behavior, where upon compression a tetratic-like phase is first observed, followed by a square phase. On the other hand, shapes with large values of s (COs, TOs and Octs) show phases with a disc-like character, where upon compression form a rotator phase followed by a crystal phase with both rotator and crystal phases exhibiting an increasing (decreasing) extent of hexagonal (square) symmetry as s increases. Interestingly, for Octs a mesophase with patches of six-fold and four-fold symmetry is observed for a small range of densities before it transitions to a hexagonal crystal. For the intermediate value of s = 0.4 (TC4s), we observe both square-like and disc-like packing in the phase behavior. Indeed, TC4s undergo a transition from isotropic to hexatic-like phase followed by a tetratic-like phase, which finally transforms into a square phase. While breaks or inflexion points in order parameters and number density along an equation of state are suggestive of the potential character the phase transitions involved, further finite-size scaling studies will be required to clarify the exact nature of these transitions.

The present work constitutes a first step towards the goal of fundamentally understanding the self-assembly of polyhedral nanoparticles at fluid-fluid interfaces. The phase behavior obtained here for purely entropic self-assembly provides a baseline for later comparisons; e.g., to understand additional entropic effects like those related to size and shape polydispersity (ubiquitous in experimental systems) and to facilitate the partial decoupling of effects brought about by the addition of enthalpic interactions. Despite the simplicity of the entropic model, some of the phases and mesophases observed here have been observed in various experiments[29-38] (and in our ongoing work), and while a direct comparison is still not possible, this concurrence nonetheless illustrates that mesophasic behavior is ubiquitous in experiments and it can occur across different types of particle interactions, potentially foretelling the preponderance of steric effects on structure. Furthermore, the entropic phase behavior found here may also prove to provide best-case scenarios for ordered assembly, which future experiments may aim to approach.

As discussed in Sec. 3.7, the adsorption energy of a particle on a fluid-fluid interface is an important contributor to the particle orientational behavior. For a single particle, the interfacial energy landscape can be modeled by using a Pieranski potential.[24] The authors of ref. 31 studied the interfacial self-assembly of hexagonal bipyramid and bifrustum shaped particles into 2D superstructures by performing MC simulations where the immersion depth and the polar angle of a particle were set according to the values estimated for the equilibrium adsorption configurations. Such constraints could be relaxed in future studies to more faithfully describe the role of metastable particle orientations. Furthermore, enthalpic particle-particle interactions can be incorporated to reflect ligand-mediated interactions present in some experimental systems, which could crucially affect the assembly behavior. Work along these lines is already under way.

TABLES

Table 1. Summary of phase behavior and comparisons to 3D bulk systems and 2D rounded squares. sc = simple cubic, dsc = distorted sc, MI = monointerlocking, bct = body-centered tetragonal, dbct = distorted bct. The comparison between our quasi-2D systems and 2D rounded squares are made at similar values of λ_{shape} and ζ.

Shape	λ_{shape}	Quasi-2D case	3D bulk case [11]	2D rounded squares [40]	
				ζ	Phases
Cubes	0.0	Tetratic-like square	Cubic mesophase* sc	0.0	Tetratic-like Square
TCs	0.35	Tetratic-like Square	sc dsc (C1)	0.33	Polycrystalline Rhombic
TC4s	0.41	Hexatic-like rotator Tetratic-like Square	Plastic hcp dsc (C0) MI dsc	0.4	Hexagonal rotator Rhombic
COs	0.43	Hexagonal rotator Distorted hexagonal	Plastic bct dbct0	0.45	Hexagonal rotator Rhombic
TOs	0.60	Hexagonal rotator Rhombic	Plastic bct** dbct1	0.59	Hexagonal rotator Rhombic
Octs	0.0	Dimorphic rotator Hexagonal crystal	- Minkowski crystal	0.0	Tetratic-like Square

*) For a narrow range of densities near the ordering transition, the particles in the cubic phase have liquid-like mobilities which could be associated with mesophasic behavior[12,13].

**) Rotator phase behavior for TOs has been detected in refs. 12 and 21 although it continuously transitions into a crystalline phase as density increases.

FIGURES
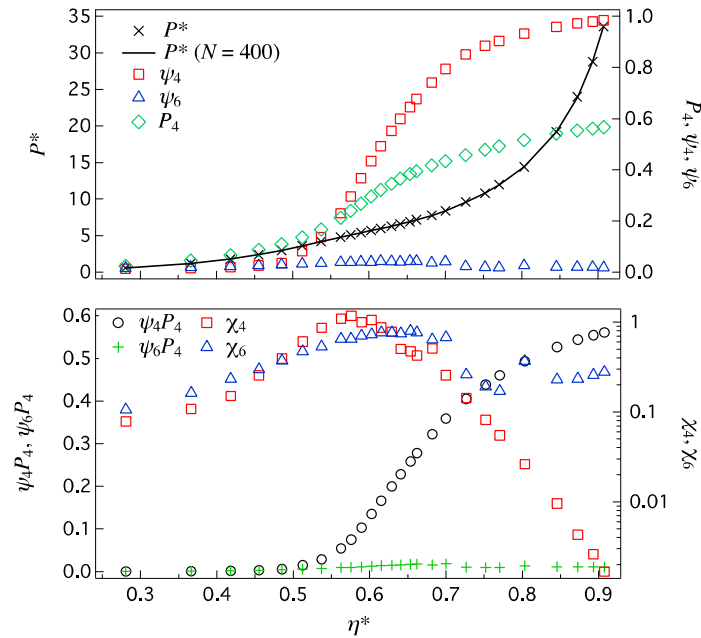
Fig. 1 Equation of state for 1600 cubes obtained by expansion runs. (Top Panel) The pressure P^*, bond orientational order parameters ψ_4 and ψ_6, and orientational order parameter P_4 as a function of reduced number density η^*. For comparison, the equation of state curve obtained from the system of $N = 400$ particles is also shown. (Bottom Panel) Cross order parameters $\psi_4 P_4$ and $\psi_6 P_4$ and susceptibilities of the bond order parameters χ_4 and χ_6 as a function of η^*. The value of η^{crys} is estimated as 0.745.
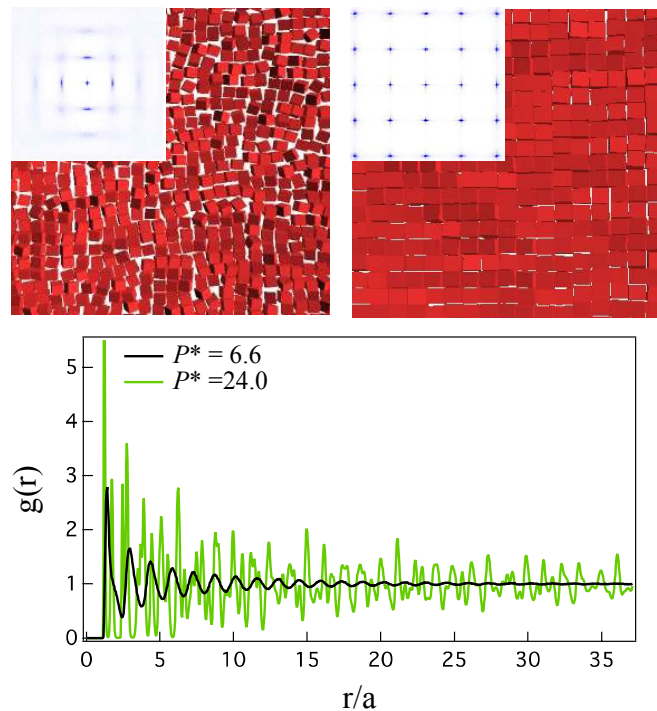
Fig. 2 (Top Panel) Representative snapshots and corresponding structure factors for a system of $N=3600$ cubes at (left) $P^*= 6.6$ (tetratic-like phase) and (right) $P^* = 24.0$ (square phase). (Bottom Panel) The radial distribution function for a system of $N = 3600$ cubes at the same two pressures.
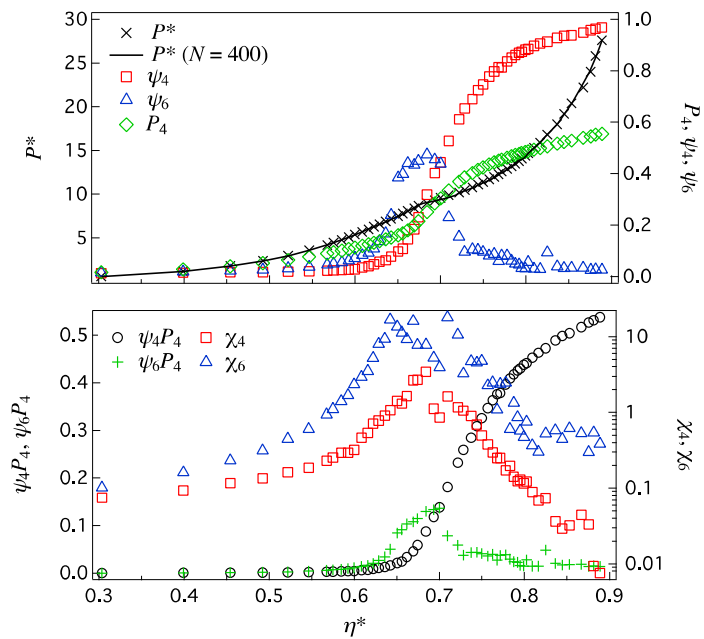
Fig. 3 Equation of state for 1600 TC4s obtained by expansion runs. Legend as in Fig. 1. The value of η^{crys} is estimated as 0.745.
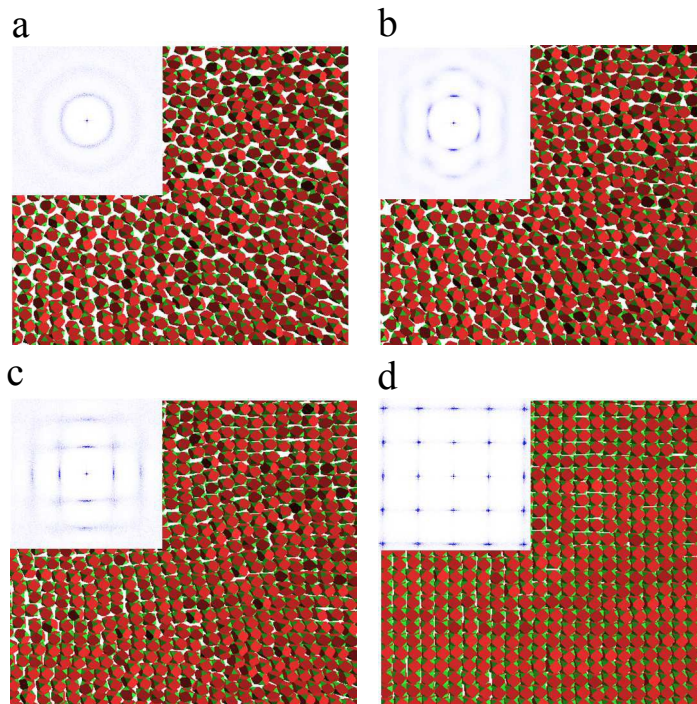
Fig. 4 Snapshots and corresponding structure factors for $N = 3600$ TC4s at (a) $P^* = 6.0$ (isotropic phase), (b) $P^* = 8.4$ (hexatic-like phase), (c) $P^* = 10.8$ (tetratic-like phase) and (d) $P^* = 24.0$ (square phase).
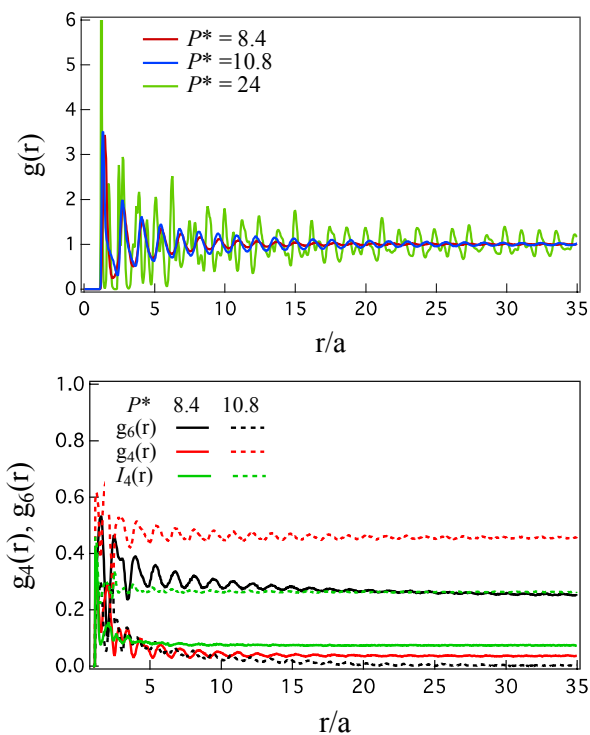
Fig. 5 Correlation functions for the system of $N = 3600$ TC4s. (Top Panel) The radial distribution function g(r) at $P^* = 8.4$ (hexatic-like phase), 10.8 (tetratic-like phase) and 24 (square phase) are shown. (Bottom Panel) The bond order correlation functions, $g_6(r)$ and $g_4(r)$, and orientational correlation function, $I_4(r)$ at $P^* = 8.4$ and 10.8 are shown.
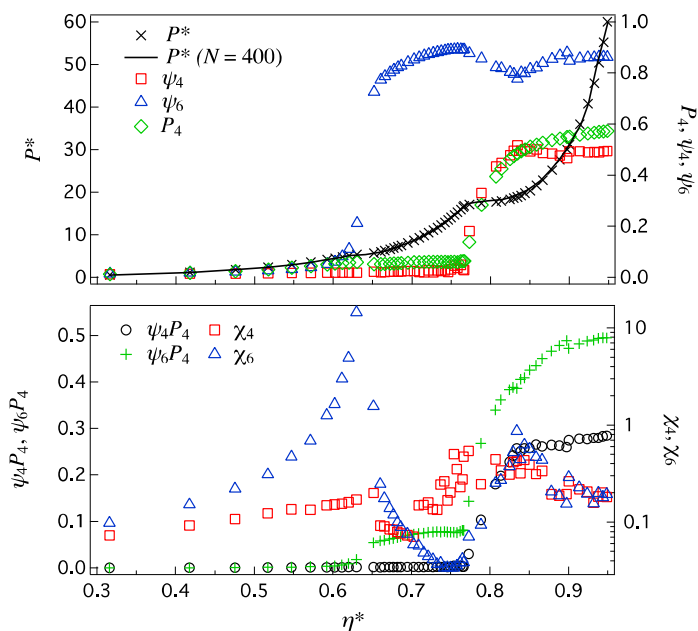
Fig. 6 Equation of state for 1600 COs obtained by expansion runs. Legend as in Fig. 1. The value of η^{crys} is estimated as 0.745.
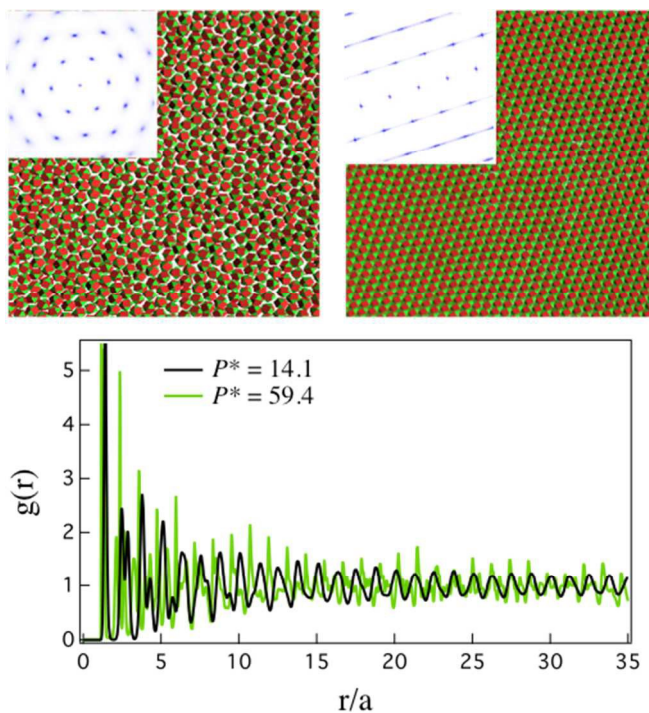
Fig. 7 (Top Panel) Representative snapshots and corresponding structure factors for a system of N=3600 COs at (left) P^*= 14.1(hexagonal rotator phase) and (right) $P^* = 59.4$ (distorted crystal phase). (Bottom Panel) The radial distribution function for a system of $N = 3600$ COs at the same two pressures.

15
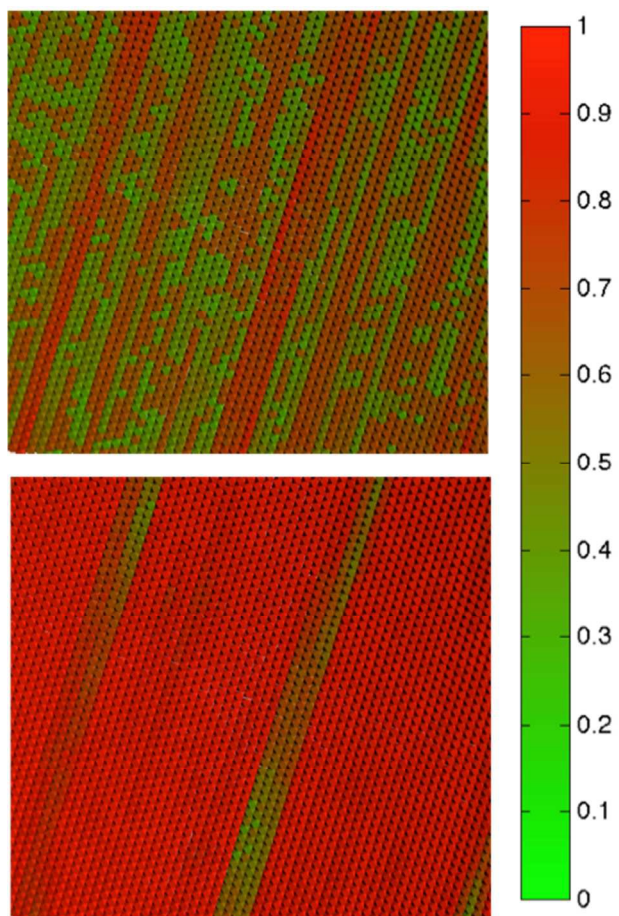
Fig. 8 Snapshot of the distorted crystal phase for the system of $N = 3600$ COs at $P^*=59.4$. (Top Panel) Particles are colored with respect to the local value of φ_4^j. (Bottom Panel) Particles are colored with respect to the local value of φ_6^j.
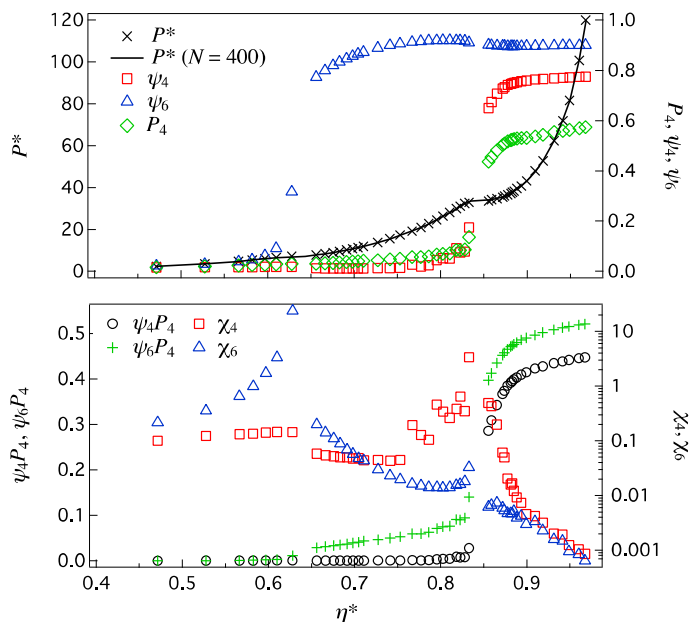
Fig. 9 Equation of state for 1600 TOs obtained by expansion runs. Legend as in Fig. 1. The value of η^{crys} is estimated as 1.05.
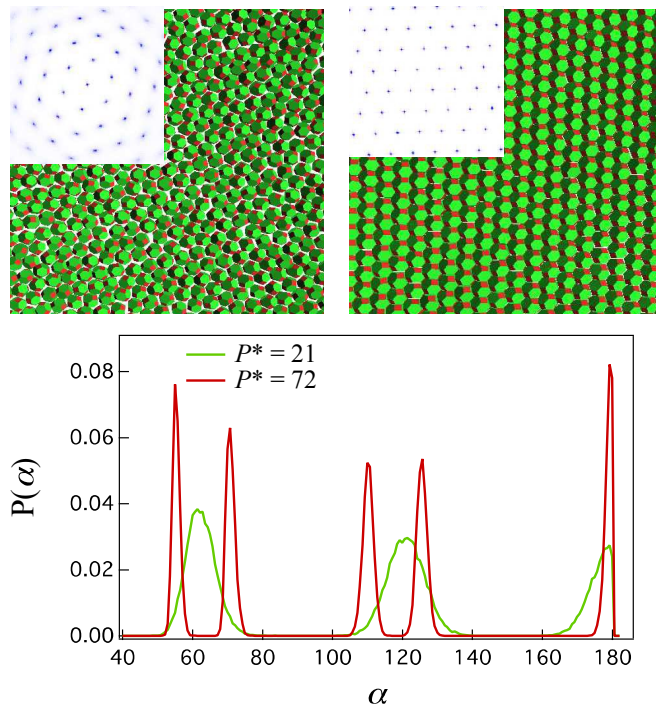
Fig. 10 (Top Panel) Representative snapshots and corresponding structure factors for a system of N=1600 TOs at (left) P^*= 21 (hexagonal rotator phase) and (right) $P^* = 72$ (rhombic phase). (Bottom Panel) Probability density function of angle, α for a system of $N = 1600$ TOs at the same two pressures.

17
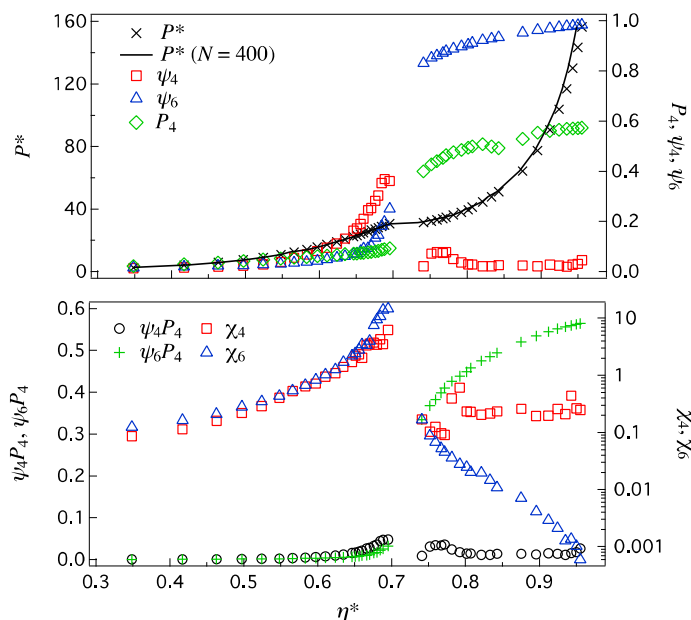
Fig. 11 Equation of state for 1600 Octs obtained by expansion runs. Legend as in Fig. 1. The value of η^{crys} is estimated as 2.247.
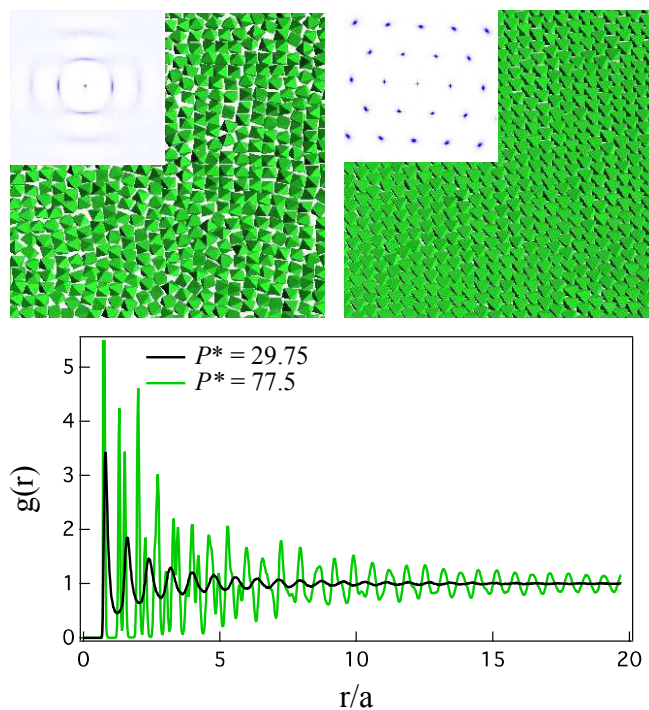
Fig. 12 (Top Panel) Representative snapshots and corresponding structure factors for a system of N=3600 Octs at (left) P^*= 29.75 (mixed phase) and (right) P^* = 77.5(hexagonal crystal phase). (Bottom Panel) The radial distribution function for a system of N = 3600 Octs at the same two pressures.
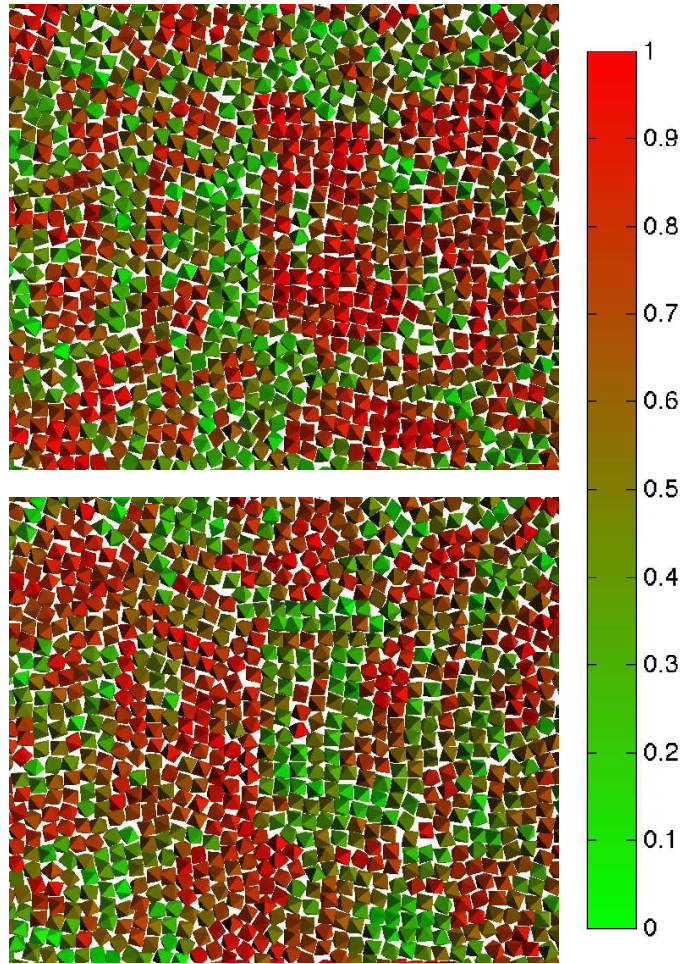
Fig. 13 Snapshot of the phase observed at $P^*= 29.75$ for the system of $N = 3600$ Octs. (Top Panel) Particles are colored with respect to the local value of φ_4^j. (Bottom Panel) Particles are colored with respect to the local value of φ_6^j.

19
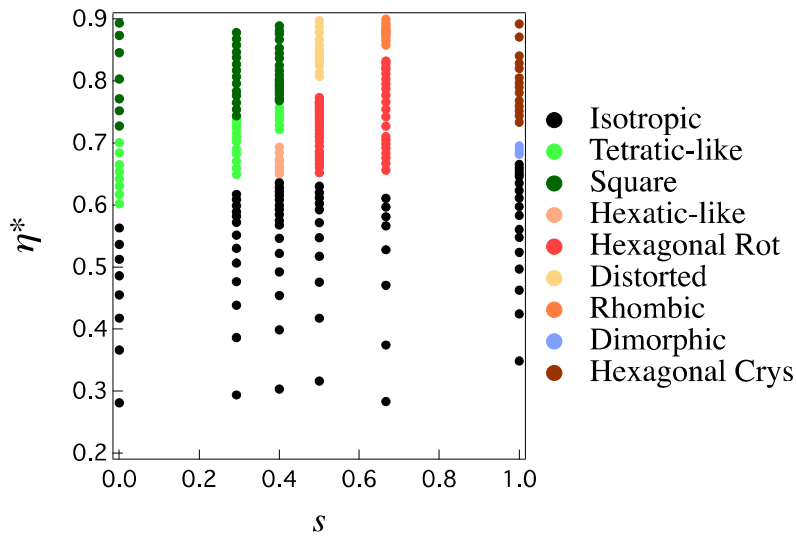
Fig. 14 Concentration vs. truncation parameter phase diagram for different shapes obtained from MC expansion runs for systems with $N = 1600$ particles.
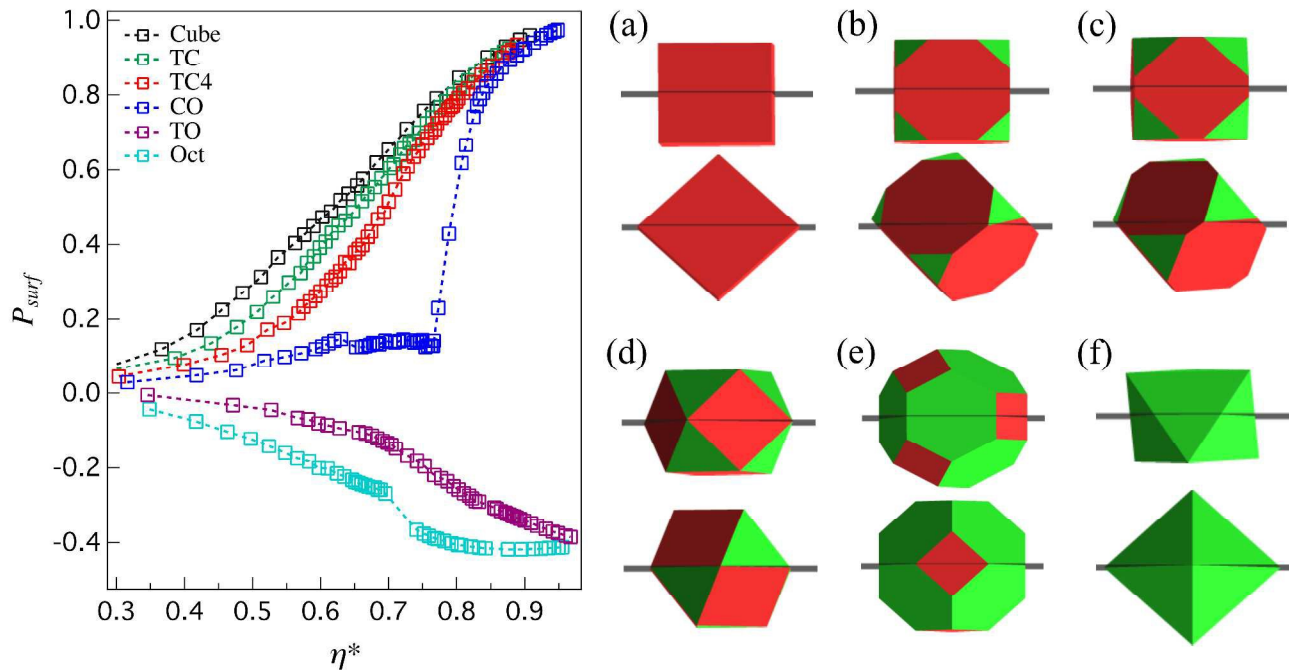
Fig. 15 Left panel: Orientational order relative to the interface, P_{surf}, as a function of η^* for different shapes. The values of P_{surf} corresponding to the single-particle most stable orientation at $\cos\theta_1 = \cos\theta_2 = 0.0$ are -0.41, -0.43, -0.42, -0.39, 1.0 and 1.0 for cube, TC, TC4, CO, TO and Oct respectively. Right panel: Snapshots showing the orientation of a particle orientation relative to the interface (horizontal line) for a cube (a), TC (b), TC4 (c), CO (d), TO (e), and Oct (f); in each case the top snapshot is for the densest packed state obtained from the entropic model and the bottom snapshot is for the most stable orientation with $\cos\theta_1 = \cos\theta_2 = 0.0$ obtained from the single-particle interfacial model ({100} facets are colored red and {111} facets are green).

References

1. E. V. Shevchenko, D. V. Talapin, N. A. Kotov, S. O'Brien, and C. B. Murray, *Nature*, 2006, **439**, 55–59.
2. D. Seo, J. C. Park, and H. Song, *J. Am. Chem. Soc.*, 2006, **128**, 14863–14870.
3. O. C. Compton and F. E. Osterloh, *J. Am. Chem. Soc.*, 2007, **129**, 7793–7798.
4. W. Niu, L. Zhang, and G. Xu, *ACS Nano*, 2010, **4**, 1987–1996.
5. J. Henzie, M. Grünwald, A. Widmer-Cooper, P. L. Geissler and P. Yang, *Nat. Mater.*, 2012, **11**, 131–137
6. N. V. Long, M. Ohtaki, M. Uchida, R. Jalem, H. Hirata, N. D. Chien, and M. Nogami, *J. Colloid Interface Sci.*, 2011, **359**, 339–350.
7. R. Gabbrielli, Y. Jiao, and S. Torquato, *Phys. Rev. E*, 2012, **86**, 041141.
8. J. H. Conway, Y. Jiao, and S. Torquato, *Proc. Natl. Acad. Sci. U.S.A.*, 2011, **108**, 11009–11012.
9. S. Torquato and Y. Jiao, *Phys. Rev. E*, 2009, **80**, 041104.
10. Y. Jiao, F. Stillinger, and S. Torquato, *Phys. Rev. E*, 2009, **79**, 041309.
11. S. Torquato and Y. Jiao, *Nature*, 2010, **460**, 876–879.
12. U. Agarwal and F. A. Escobedo, *Nat. Mater.*, 2011, **10**, 230–235.
13. U. Agarwal and F. A. Escobedo, *J. Chem. Phys.*, 2012, **137**, 024905.
14. P. F. Damasceno, M. Engel, and S. C. Glotzer, *ACS Nano*, 2012, **6**, 609–614.
15. F. Smallenburg, L. Filion, M. Marechal, and M. Dijkstra, *Proc. Natl. Acad. Sci. U.S.A.*, 2012, **109**, 17886–17890.
16. P. F. Damasceno, M. Engel, and S. C. Glotzer, *Science*, 2012, **337**, 453–457.
17. A. P. Gantapara, J. de Graaf, R. van Roij, and M. Dijkstra, *Phys. Rev. Lett.*, 2013, **111**, 015501.
18. M. Marechal and H. Löwen, *Phys. Rev. Lett.*, 2013, **110**, 137801.
19. M. R. Khadilkar, U. Agarwal, and F. A. Escobedo, *Soft Matter*, 2013, **9**, 11557-11567.
20. M. R. Khadilkar and F. A. Escobedo, *Phys. Rev. Lett.*, 2014, **113**, 165504.
21. V. Thapar and F. A. Escobedo, *Phys. Rev. Lett.*, 2014, **112**, 048301.
22. S. U. Pickering, *J. Chem. Soc. Trans.*, 1907, **91**, 2001-2021.
23. W. Ramsden, *Proc. R. Soc. London, Ser. A*, 1903, **72**, 156-164.
24. P. Pieranski, *Phys. Rev. Lett.*, 1980, **45**, 569-572.
25. N. Bowden, A. Terfort, J. Carbeck and G. M. Whitesides, *Science*, 1997, **276**, 233–235
26. N. Bowden, F. Arias, T. Deng, and G. M. Whitesides, *Langmuir*, 2001, **17**, 1757–1765.
27. F. Bresme and M. Oettel, *J. Phys.: Condens. Matter*, 2007, **19**, 413101.
28. S. Kutuzov, J. He, R. Tangirala, T. Emrick, T. P. Russell, and A. Böker, *Phys. Chem. Chem. Phys.*, 2007, **9**, 6351–6358.
29. W. J. Baumgardner, K. Whitham, and T. Hanrath, *Nano Lett.*, 2013, **13**, 3225–3231.
30. W. H. Evers, B. Goris, S. Bals, M. Casavola, J. de Graaf, R. van Roij, M. Dijkstra, and D. Vanmaekelbergh, *Nano Lett.*, 2013, **13**, 2317–2323.
31. W. van der Stam, A. P. Gantapara, Q. A. Akkerman, G. Soligno, J. D. Meeldijk, R. van Roij, M. Dijkstra, and C. de Mello Donega, *Nano Lett.*, 2014, **14**, 1032–1037.
32. S. Dasgupta, M. Katava, M. Faraj, T. Auth, and G. Gompper, *Langmuir*, 2014, **30**, 11873–11882.
33. N. Bizmark, M. A. Ioannidis, and D. E. Henneke, *Langmuir*, 2014, **30**, 710–717.
34. G. B. Davies, T. Krüger, P. V. Coveney, J. Harting, and F. Bresme, *Soft Matter*, 2014, **10**, 6742–6748.
35. S. Razavi, I. Kretzschmar, J. Koplik, and C. E. Colosqui, *J. Chem. Phys.*, 2014, **140**, 014904.
36. S. Srivastava, D. Nykypanchuk, M. Fukuto, J. D. Halverson, A. V. Tkachenko, K. G. Yager, and O. Gang, *J. Am. Chem. Soc.*, 2014, **136**, 8323–8332.
37. J. J. Choi, K. Bian, W. J. Baumgardner, D.-M. Smilgies, and T. Hanrath, *Nano Lett.*, 2012, **12**,

4791–4798.

38. T. Hanrath, *J. Vac. Sci. Technol. A*, 2012, **30**, 030802.
39. E. Kalesaki, W. H. Evers, G. Allan, D. Vanmaekelbergh and C. Delerue, *Phys. Rev. B*, 2013, **88**, 115431.
40. C. Avendaño and F. A. Escobedo, *Soft Matter*, 2012, **8**, 4675.
41. N. Metropolis, A. W. Rosenbluth, M. N. Rosenbluth, A. H. Teller, and E. Teller, *J. Chem. Phys.*, 1953, **21**, 1087.
42. E. G. Golshtein and N. V. Tretyakov, *Modified Lagrangians and monotone maps in optimization*, Wiley, New York, 1996
43. B. S. John, C. Juhlin, and F. A. Escobedo, *J. Chem. Phys.*, 2008, **128**, 044909.
44. A. Jaster, *Phys. Rev. E*, 1999, **59**, 2594–2602.
45. H. Weber, D. Marx and K. Binder, *Phys. Rev. B: Condens. Matter*, 1995, **51**, 14636.
46. Y. Han, N. Y. Ha, A. M. Alsayed, and A. G. Yodh, *Phys. Rev. E*, 2008, **77**, 041406.
47. K. W. Wojciechowski and D. Frenkel, *Comp. Met. Sci. Technol.*, 2004, **10**, 235.
48. See Supplementary Material for details regarding the phase behavior of truncated cubes (TCs), potentials of mean force, adsorption energy of single particle confined to a fluid-fluid interface and orientational order relative to an interface.
49. H. Friedrich, C. J. Gommes, K. Overgaag, J. D. Meeldijk, W. H. Evers, B. de Nijs, M. P. Boneschanscher, P. E. de Jongh, A. J. Verkleij, K. P. de Jong, A. van Blaaderen and D. Vanmaekelbergh, *Nano Lett.*, 2009, **9**, 2719–2724.
50. D. K. Smith, B. Goodfellow, D. M. Smilgies and B. A. Korgel, *J. Am. Chem. Soc.*, 2009, **131**, 3281–3290.

Soft Matter